J. Plasma Phys. (2025), *vol*. 91, E62
doi:10.1017/S002237782500025X

Suppression of the collisionless tearing mode by flow shear: implications for reconnection onset in the Alfvénic solar wind

A. Mallet[1], S. Eriksson[2], M. Swisdak[3] and J. Juno[4]

[1]Space Sciences Laboratory, University of California, Berkeley, CA 94720, USA
[2]Laboratory for Atmospheric and Space Physics, University of Colorado, Boulder, CO 80303, USA
[3]Institute for Research in Electronics and Applied Physics, University of Maryland, College Park, MD 20742, USA
[4]Princeton Plasma Physics Laboratory, Princeton, NJ 08543, USA

Corresponding author: A. Mallet, alfred.mallet@berkeley.edu

(Received 2 December 2024; revision received 4 February 2025; accepted 25 February 2025)

We analyse the collisionless tearing mode instability of a current sheet with a strong shear flow across the layer. The growth rate decreases with increasing shear flow, and is completely stabilised as the shear flow becomes Alfvénic. We also show that, in the presence of strong flow shear, the tearing mode growth rate decreases with increasing background ion-to-electron temperature ratio, the opposite behaviour to the tearing mode without flow shear. We find that even a relatively small flow shear is enough to dramatically alter the scaling behaviour of the mode, because the growth rate is small compared with the shear flow across the ion scales (but large compared with shear flow across the electron scales). Our results may explain the relative absence of reconnection events in the near-Sun Alfvénic solar wind observed recently by NASA's Parker Solar Probe.

Keywords: plasma instabilities, space plasma physics

1. Introduction

Magnetic reconnection is a fundamental plasma physics process, involving a topological rearrangement of the magnetic field, and accompanied by the conversion of magnetic energy into bulk plasma flow and heat. Reconnection occurs in a wide range of contexts, for example solar flares (Yan *et al*. 2022), at planetary magnetopauses (Paschmann, Øieroset & Phan 2013), in magnetic confinement fusion devices (Kadomtsev 1975; Zanini *et al*. 2020) and other laboratory plasmas (Ji *et al*. 2023) and in current sheets ubiquitous in many space and astrophysical environments (Eriksson *et al*. 2022, 2024).

Here, we are specifically motivated by observations of current sheets in the near-Sun solar wind, currently being explored *in situ* for the first time by NASA's Parker Solar Probe (PSP) spacecraft. While such sheets are observed essentially ubiquitously (Vasko *et al*. 2022; Lotekar *et al*. 2022), only a small fraction actually

reconnect (Eriksson *et al*. 2022). In the Alfvénic solar wind (D'Amicis & Bruno 2015; D'Amicis *et al*. 2021), the fluctuations are close to Alfvén waves propagating away from the Sun, with velocity fluctuations $\delta u \approx \pm \delta b$, $\delta b = \delta B/\sqrt{4\pi n_i m_i}$ being the magnetic field fluctuation in velocity units. An even more pronounced absence of reconnection events has been observed in this type of solar wind (Phan *et al*. 2020; Fargette *et al*. 2023; Eriksson *et al*. 2024), suggesting that the quasi-Alfvénic velocity shear accompanying the magnetic shear across current sheets suppresses the onset of reconnection, as observed in steady-state nonlinear reconnection simulations (Cassak 2011). Here, we develop a linear theory to describe the suppression of reconnection onset by such a flow shear.

Many numerical studies of reconnection begin with a kinetic-scale current sheet: for example, the GEM reconnection challenge problem (Birn *et al*. 2001) has a current sheet with a width comparable to $\mathrm{d}_i = c/\omega_{pi}$, where $\omega_{pi} = (4\pi n_i Z^2 e^2/m_i)^{1/2}$ is the ion plasma frequency, with $Z = q_i/e$. With this set-up, reconnection proceeds rapidly from the outset. However, in many of the natural systems mentioned above, reconnection occurs as part of a bursty, two-time-scale process: first a long, quiescent phase in which magnetic energy builds up in thinning current sheets, followed by an extremely rapid disruption as reconnection occurs.

Recently, new models of reconnection onset that explain this property have been developed (Pucci & Velli 2014; Uzdensky & Loureiro 2016; Tolman, Loureiro & Uzdensky 2018). On large scales, ideal dynamics leads to the progressive 'thinning' of the current sheet width a, for example via the Chapman–Kendall collapse (Chapman & Kendall 1963), on a characteristic (ideal) time scale $T(a)$. This can be compared with the growth rate of the tearing mode (the linear stage of reconnection), $\gamma(a)$: only when $\gamma(a)T(a) \gtrsim 1$ will reconnection onset occur: at which point, the ideal dynamics is disrupted and the current sheet is usually destroyed. This model has also been applied to turbulence, where T can be identified as the nonlinear time scale T_{nl}, whose scaling depends on the details of the turbulence (Mallet *et al*. 2017*a*,*b*; Loureiro & Boldyrev 2017*a*,*b*; Comisso *et al*. 2018).

To apply this model to the highly sheared current sheets observed by PSP, we need to understand the scalings of both γ and T in the presence of strong flow shear, neither of which are currently well understood. Here, we focus on the former problem, and develop a new analytic theory for the collisionless tearing mode with significant flow shear, $\delta u \sim \delta b = \delta B/\sqrt{4\pi n_i m_i}$, determining the growth rate γ as a function of the physical parameters. We find that flow shear strongly suppresses the tearing instability, with the growth rate proportional to $1 - \alpha^2$, where $\alpha = \delta u/\delta b$: as $\alpha \to 1$, corresponding to Alfvénic flow shear, the growth rate of the tearing mode vanishes (for $\alpha > 1$, we would have instead the ideal Kelvin–Helmholtz instability, whose growth rate is proportional to $\sqrt{\alpha^2 - 1}$: we will not comment further on this instability here). Finally, we discuss how our results might apply to the PSP observations.

1.1. *Tearing mode without shear flow*

To compare with the new results we will find in our calculation, we first present an overview of the collisionless tearing mode scalings without equilibrium flow shear.[1]

[1]Specifically, the scalings at low β with a strong guide field: these can be found from (2.13)–(2.15) without the flow shear terms, i.e. with $\alpha = 0$. A clear and concise derivation, along with references to previous works, is given by Zocco & Schekochihin 2011.

We assume that the current sheet normal is in the $\hat{x}$ direction, with reconnecting field $v_{Ay} = \delta b = \delta B/\sqrt{4\pi n_{0i} m_i}$, the wavenumber k of the tearing mode both in the $\hat{y}$ direction and a strong constant guide field $B_0 \gg \delta B$ pointing in the $\hat{z}$ direction. The growth rate is given by

$$\frac{\gamma_0 a}{v_{Ay}} \sim \begin{cases} k\Delta' \mathrm{d}_e \rho_s \sqrt{1+\tau/Z}, & \Delta'\delta_{in} \ll 1 \\ k d_e^{1/3} \rho_s^{2/3} \sqrt{1+\tau/Z}, & \Delta'\delta_{in} \gg 1, \end{cases} \tag{1.1}$$

where $\rho_s = \sqrt{ZT_{0e}/m_i}/\Omega_i$ is the ion sound radius and $\mathrm{d}_e = c/\omega_{pe}$ is the electron inertial length, with $Z = q_i/e$, $\tau = T_{0i}/T_{0e}$, $\omega_{pe} = (4\pi n_{0e} e^2/m_e)^{1/2}$ the electron plasma frequency and $\Omega_i = ZeB_0/m_i c$ the ion gyrofrequency (Zocco & Schekochihin 2011). Here, Δ' is a measure of the ideal discontinuity (see § 3 for details), with $\Delta' > 0$ required for instability, while $\delta_{in} \ll a$ is the inner layer width over which the microphysics becomes important. The explicit form of δ_{in} depends on the regime, but is not needed here. We refer the reader to Zocco & Schekochihin (2011) for further details. The parameter Δ' depends on k in a way that depends on the specific equilibrium profile (Boldyrev & Loureiro 2018): for $ka \ll 1$, we have $\Delta' a \propto (ka)^{-n}$ with $n = 1$ for a Harris-type equilibrium (Harris 1962) with $f(x/a) = \tanh(x/a)$ and $n = 2$ for $f(x/a) = \sin(x/a)$. For $\Delta'\delta_{in} \ll 1$, the growth rate γ_0 decreases with k, while at $\Delta'\delta_{in} \gg 1$, γ_0 increases with k. The maximum growth rate and wavenumber at which it is attained may be found by equating the two expressions in (1.1)

$$\frac{\gamma_{0tr} a}{v_{Ay}} \sim \frac{\mathrm{d}_e^{1/3+2/(3n)} \rho_s^{2/3+1/(3n)} \sqrt{1+\tau/Z}}{a^{1+1/n}}, \quad k_{0tr} a \sim \frac{\mathrm{d}_e^{2/(3n)} \rho_s^{1/(3n)}}{a^{1/n}}. \tag{1.2}$$

For $n = 1$ the growth rate in the $\Delta'\delta_{in} \ll 1$ case does not depend on k, and so the growth rate is the same for all $k > k_{0tr}$: for $n = 2$ this is not the case. In the calculation that follows, we will find that these scalings are strongly affected by the presence of even relatively modest flow shear.

2. Equations

We will use the kinetic reduced electron heating model (KREHM) equations (Zocco & Schekochihin 2011), in the collisionless limit. These equations are derived from gyrokinetics (and thus assume low-frequency fluctuations $\omega \ll \Omega_i$ and a strong guide field, $\delta B/B_0 \ll 1$) in the limit of small $\beta_e = 8\pi n_{0e} T_{0e}/B_0^2$, and, assuming no variations in the $\hat{z}$ direction, may be written

$$\frac{d}{\mathrm{d}t}(1-\hat{\Gamma}_0)\Phi = -\frac{1}{2}\rho_i^2 \left\{\Psi, \nabla_\perp^2 \Psi\right\}, \tag{2.1}$$

$$\frac{d}{\mathrm{d}t}(\Psi - d_e^2 \nabla_\perp^2 \Psi) = \left\{\Psi, \frac{Z}{\tau}(1-\hat{\Gamma}_0)\Phi - \frac{c}{eB_0}\delta T_{\parallel e}\right\}, \tag{2.2}$$

$$\frac{\mathrm{d}g_e}{\mathrm{d}t} + \frac{v_\parallel}{v_A}\left\{\Psi, g_e - \frac{\delta T_{\parallel e}}{T_{0e}} F_{0e}\right\} = -\frac{1}{\Omega_i}\left(1 - \frac{2v_\parallel^2}{v_{the}^2}\right) F_{0e} \left\{\Psi, \nabla_\perp^2 \Psi\right\}. \tag{2.3}$$

where the Poisson bracket is $\{f, g\} = \hat{z} \cdot (\nabla_\perp f \times \nabla_\perp g)$, and the ion gyroradius is $\rho_i = v_{thi}/\Omega_i$, with $v_{thi} = \sqrt{2T_{0i}/m_i}$ the ion thermal speed . Here, B_0 is again the (strong) guide magnetic field in the out-of-plane $\hat{z}$ direction, F_{0e} is the equilibrium Maxwellian electron distribution function, and

$$\frac{\mathrm{d}}{\mathrm{d}t} = \frac{\partial}{\partial t} + \{\Phi, \ldots\}. \tag{2.4}$$

The equations have been written in different variables to Zocco & Schekochihin (2011)

$$\Phi = \frac{c}{B_0}\phi, \quad \Psi = -\frac{A_\parallel}{\sqrt{4\pi m_i n_{0i}}}, \tag{2.5}$$

chosen to be notationally similar to reduced magnetohydrodynamics (RMHD): ϕ is the electric potential and $A_\parallel$ is the parallel magnetic vector potential, while the perpendicular (to $\hat{z}$) magnetic field (in velocity units) is $b_\perp = \hat{z} \times \nabla_\perp \Psi$ and the $E \times B$ velocity is $u_{E\times B} = \hat{z} \times \nabla_\perp \Phi$. The operator $\hat{\Gamma}_0$ is the inverse Fourier transform of

$$\Gamma_0(k_\perp^2 \rho_i^2/2) = I_0(k_\perp^2 \rho_i^2/2) e^{-k_\perp^2 \rho_i^2/2}, \tag{2.6}$$

where I_0 is the modified Bessel function: at large and small scales, we have

$$1 - \hat{\Gamma}_0 \approx \begin{cases} -\frac{\rho_i^2}{2}\nabla_\perp^2, & \rho_i^2 \nabla_\perp^2 \ll 1 \\ 1, & \rho_i^2 \nabla_\perp^2 \gg 1. \end{cases} \tag{2.7}$$

In (2.1) we have already substituted

$$\frac{\delta n_e}{n_{0e}} = -\frac{2}{\rho_i^2 \Omega_i}(1 - \hat{\Gamma}_0)\Phi = \frac{\delta n_i}{n_{0i}}, \tag{2.8}$$

for the density fluctuations. Equation (2.3) evolves the reduced parallel electron distribution function g_e, defined in terms of the perturbed parallel electron distribution function δf_e as

$$g_e = \delta f_e - \left[\frac{\delta n_e}{n_{0e}} + \frac{2 v_\parallel u_{\parallel e}}{v_{the}^2}\right] F_{0e}. \tag{2.9}$$

The parallel electron temperature fluctuation is given by the second moment of g_e

$$\frac{\delta T_{\parallel e}}{T_{0e}} = \frac{1}{n_{0e}} \int d^3 v \frac{2 v_\parallel^2}{v_{the}^2} g_e. \tag{2.10}$$

The KREHM is designed to be a set of equations appropriate for studying reconnection: the equations contain a rigorous treatment of electron heating via the electron kinetic equation (2.3), the dispersion at the ion scales (ρ_i and $\rho_s = \rho_i \sqrt{Z/2\tau}$), important for achieving fast reconnection (Shay *et al*. 2001) and also the flux unfreezing at the electron inertial-scale d_e. This model cannot be expected to apply to all the current sheets observed in the solar wind: in particular, the assumptions that $\beta \ll 1$ and $\delta B/B_0 \ll 1$ are often not satisfied, nor do we attempt to model sheared parallel flow or density gradients across the current sheet. However, it will allow us to make progress in understanding reconnection onset in the near-Sun solar wind.

2.1. *Equilibrium and linearised equations*

Our chosen equilibrium is

$$\Phi_0 = \alpha \Psi_0, \quad b_{0y} = v_{Ay} f(x/a) = \partial_x \Psi_0, \tag{2.11}$$

where we will be especially interested in the case where the shear flow in the $\hat{y}$ direction is comparable to the reconnecting magnetic field, $\alpha \sim 1$. As in § 1.1, we

have the current sheet normal in the $\hat{x}$ direction and both the reconnecting field and wavenumber in the $\hat{y}$ direction. We also assume that the equilibrium length scale is large compared with ion and electron scales, $a \gg \rho_i \sim \rho_s \gg \mathrm{d}_e$. We have also implicitly assumed that $u_{0y}, b_{0y} \ll v_A$, so we are limited to guide-field reconnection. Relaxing this assumption is not possible with the KREHM equations, which assume that there are no flows on the same level as the background (guide) magnetic field B_0. Linearising (2.1)–(2.3) and assuming fluctuations of the form

$$\delta\Phi = \Phi(x)\exp(iky + \gamma t), \quad \delta\Psi = \Psi(x)\exp(iky + \gamma t), \tag{2.12}$$

and that $k^{-1} \gg \rho_i, \mathrm{d}_e$, we obtain

$$(\gamma + i\alpha k v_{Ay} f)(1 - \hat{\Gamma}_0)\Phi + \frac{1}{2} i\alpha k v_{Ay}\rho_i^2 f''\Phi = -\frac{1}{2} ikv_{Ay} f \rho_i^2 \left[\Psi'' - k^2\Psi - \frac{f''}{f}\Psi\right], \tag{2.13}$$

$$(\gamma + i\alpha k v_{Ay} f)(\Psi - \mathrm{d}_e^2\Psi'') = ikv_{Ay} f\left[\left(1 + \frac{Z}{\tau}(1 - \hat{\Gamma}_0)\right)\Phi - \frac{c}{eB_0}\delta T_{\parallel e}\right], \tag{2.14}$$

$$(\gamma + i\alpha k v_{Ay} f) g_e + ikv_{Ay} f \frac{v_\parallel}{v_A}\left(g_e - \frac{\delta T_{\parallel e}}{T_{0e}} F_{0e}\right) = - \frac{1}{\Omega_i} ikv_{Ay} f \left(1 - \frac{2v_\parallel^2}{v_{the}^2}\right) F_{0e}\left[\Psi'' - k^2\Psi - \frac{f''}{f}\Psi\right]. \tag{2.15}$$

We first solve the linearised kinetic equation (2.15) for g_e, integrating according to (2.10) to find

$$\frac{\delta T_{\parallel e}}{T_{0e}} = -\frac{2}{\Omega_i}\frac{v_A}{v_{the}}\frac{Z(\zeta) + \zeta Z'(\zeta)}{Z'(\zeta)}\left(\Psi'' - k^2\Psi - \frac{f''}{f}\Psi\right), \tag{2.16}$$

where

$$\zeta = \left[\frac{i\gamma}{kv_{Ay} f} - \alpha\right]\frac{v_A}{v_{the}}, \tag{2.17}$$

and $Z(\zeta)$ is the plasma dispersion function, with $Z'(\zeta) = -2(1 + \zeta Z(\zeta))$. Using (2.13),

$$\frac{c}{eB_0}\delta T_{\parallel e} = -(G - 1)\frac{Z}{\tau}(1 - \hat{\Gamma}_0)\Phi, \tag{2.18}$$

where we have dropped a term since $\rho_s^2 f''/f \ll 1$, and

$$G = 2\left(\zeta^2 - \frac{1}{Z'(\zeta)}\right). \tag{2.19}$$

For $\zeta \to \infty$, $G \to 3$ (adiabatic electrons), while as $\zeta \to 0$, $G \to 1$ (isothermal electrons). Inserting (2.18) into (2.14), we obtain

$$(\gamma + i\alpha k v_{Ay} f)(\Psi - d_e^2\Psi'') = ikv_{Ay} f\left[\left(1 + G\frac{Z}{\tau}(1 - \hat{\Gamma}_0)\right)\Phi\right]. \tag{2.20}$$

We will solve (2.13) and (2.20) in the 'outer region' $x \sim a$ and in the 'inner region' close to $x = 0$. Compared with the resistive magnetohydrodynamics (MHD) case

(Chen & Morrison 1989), the main differences are, first, that we have the electron inertia term involving d_e allowing reconnection instead of resistivity, and second, the terms involving $1-\hat{\Gamma}_0$ which encode the ion-scale behaviour. Since there are two microscales in the problem, ρ_s (or ρ_i) and $\mathrm{d}_e \ll \rho_s$, there will be nested ion and electron boundary layers. Because γ is real, the real and imaginary parts of the eigenmodes will be even and odd respectively around $x=0$, and it will turn out that the imaginary part is small compared with the real part.

3. Outer region

Here, $x \sim a \sim (f'/f)^{-1} \sim k^{-1} \gg \rho_s, \mathrm{d}_e$. On these scales

$$1-\hat{\Gamma}_0 \approx -\frac{1}{2}\rho_i^2\nabla_\perp^2 \ll 1, \tag{3.1}$$

so it may be neglected in (2.20) (but not in 2.13, where all the terms are at least this small). Assuming $\gamma \ll k v_{\mathrm{A}y}$, we may also neglect the growth terms. (2.20) becomes

$$\Phi = \alpha\Psi, \tag{3.2}$$

and inserting this into (2.13), we obtain

$$(1-\alpha^2)f[\Psi'' - k^2\Psi - (f''/f)\Psi] = 0, \tag{3.3}$$

so that the outer solution for Ψ is the same as in the MHD tearing mode. As $x \to 0$, $\partial_x \gg k$ and $f \approx x/a$, and of the outer equation all we are left with is $\Psi'' = 0$, whence the real and imaginary parts are

$$\begin{aligned} varPsi_R &\to \Psi_{\infty R}\left(1+\frac{1}{2}\Delta'|x|\right), \quad x \to 0, \\ \Psi_I &\to \Psi_{\infty I}\left(\frac{1}{2}\Delta' x \pm 1\right), \quad x \to 0, \end{aligned} \tag{3.4}$$

defining $\Delta' = [\Psi']_{-0}^{+0}/\Psi(0)$, the discontinuity in the outer solution's magnetic field.

4. Inner region

In the inner region, of width $\delta_{in} \ll a$, the ion- and electron-scale effects become important. Here, $x \ll a$, $f \approx x/a$ and $\partial^2/\partial x^2 \gg k^2, f''/f$. Defining

$$\delta = \frac{\gamma a}{k v_{Ay}}, \tag{4.1}$$

we obtain the inner region equations

$$(\delta + i\alpha x)\,(1-\hat{\Gamma}_0)\Phi = -\frac{1}{2}ix\rho_i^2\Psi'', \tag{4.2}$$

$$(\delta + i\alpha x)\,(\Psi - \mathrm{d}_e^2\Psi'') = ix\left[\Phi + G\frac{Z}{\tau}(1-\hat{\Gamma}_0)\Phi\right]. \tag{4.3}$$

We need to deal with the non-local operator $1-\hat{\Gamma}_0$: substituting (4.2) into (4.3) we obtain

$$(\delta + i\alpha x)\,(\Psi - \mathrm{d}_e^2\Psi'') = ix\Phi + x^2 G\rho_s^2\frac{\Psi''}{\delta + i\alpha x}, \tag{4.4}$$

but we still need to calculate $1-\hat{\Gamma}_0$ to solve (4.2) itself. One simplification is to take cold ions: as $\rho_i^2\partial_x^2 \to 0$, $1-\hat{\Gamma}_0 \to -(1/2)\rho_i^2\partial_x^2$ and we recover a MHD-like version of (4.2). Instead, following Pegoraro & Schep (1986) and more recently Zocco & Schekochihin (2011), we incorporate the hot-ion response (non-rigorously) by using the Padé approximant

$$1-\hat{\Gamma}_0 \approx \frac{-(1/2)\rho_i^2\partial_x^2}{1-(1/2)\rho_i^2\partial_x^2}. \tag{4.5}$$

Then, (4.2) becomes

$$\Phi'' = \frac{ix\Psi''}{\delta+i\alpha x} - \frac{1}{2}i\rho_i^2\left(\frac{x\Psi''}{\delta+i\alpha x}\right)''. \tag{4.6}$$

We now rescale our equations by the inner length scale δ_{in}, to be determined later: writing

$$\xi = \frac{x}{\delta_{in}}, \quad \lambda = \frac{\delta}{\delta_{in}}, \quad \epsilon = \frac{d_e}{\rho_s} \ll 1, \tag{4.7}$$

and with $'$ now denoting differentiation by ξ, (4.6) and (4.4) become

$$\Phi'' = \frac{i\xi\Psi''}{\lambda+i\alpha\xi} - \frac{1}{2}i\frac{\rho_i^2}{\delta_{in}^2}\left(\frac{\xi\Psi''}{\lambda+i\alpha\xi}\right)'', \tag{4.8}$$

$$(\lambda+i\alpha\xi)\Psi - i\xi\Phi = \frac{\rho_s^2}{\delta_{in}^2}\left[G\xi^2 + (\lambda+i\alpha\xi)^2\epsilon^2\right]\frac{\Psi''}{\lambda+i\alpha\xi}, \tag{4.9}$$

where the argument of $G(\zeta)$ (see equation (2.19)) is

$$\zeta = \frac{1}{\sqrt{2}}\epsilon\left(\frac{i\lambda}{\xi}-\alpha\right). \tag{4.10}$$

The electron inertia term in (4.9) becomes important when $\xi \sim \lambda\epsilon$ ($x \sim \delta\epsilon$): this is also the scale below which the electrons are no longer isothermal, i.e. when $\zeta \sim 1$ so that $G(\zeta)$ starts to differ from 1. We are free to choose δ_{in} to be of the same order as the ion scale, $\delta_{in} \sim \rho_s$, and anticipate $\lambda \sim \epsilon \ll 1$.

4.1. *Ion layer*

We first solve the equations on the ion scales, $\xi \sim 1$. Since $\lambda \ll \alpha \sim 1$, to lowest order the equations are

$$\Phi'' = \frac{1}{\alpha}\left(\Psi'' - \frac{1}{2}\frac{\rho_i^2}{\delta_{in}^2}\Psi''''\right), \tag{4.11}$$

$$\alpha\Psi - \Phi = -\frac{1}{\alpha}\frac{\rho_s^2}{\delta_{in}^2}\Psi''. \tag{4.12}$$

The solution that matches onto the outer layer solution (3.4) is

$$\Psi_i = \Psi_\infty\left(1+\frac{1}{2}\Delta'\delta_{in}\xi\right) + C_i e^{-\xi}, \tag{4.13}$$

$$\Phi_i = \alpha\Psi_\infty\left(1+\frac{1}{2}\Delta'\delta_{in}\xi\right) + \frac{1}{\alpha}C_i e^{-\xi}\left[1-\frac{1-\alpha^2}{1+Z/\tau}\right], \tag{4.14}$$

where we have set

$$\delta_{in} = \frac{\rho_s\sqrt{1+\tau/Z}}{\sqrt{1-\alpha^2}}. \tag{4.15}$$

It is worth noticing that the solution for Φ_i is very different from the tearing mode without shear as $\xi \to \infty$, to match the outer solution (3.4), which is also very different from its equivalent with $\alpha = 0$, since the flow shear dominates over the growth rate on the large equilibrium scales. Moreover, it is clear that (4.11) depends strongly on the ratio of ρ_i to ρ_s, i.e. on τ. These two facts will conspire to change the τ-dependence of the growth rate from the case with no shear flow (1.1). As $\xi \to 0$, we have

$$\Psi_i \to \Psi_\infty + C_i + \left(\frac{1}{2}\Delta'\delta_{in}\Psi_\infty - C_i\right)\xi, \tag{4.16}$$

$$\Phi_i \to \alpha\Psi_\infty + \frac{1}{\alpha}C_i\left[1 - \frac{1-\alpha^2}{1+Z/\tau}\right] + \left(\frac{1}{2}\alpha\Delta'\delta_{in}\Psi_\infty - \frac{1}{\alpha}C_i\left[1 - \frac{1-\alpha^2}{1+Z/\tau}\right]\right)\xi. \tag{4.17}$$

4.2. *Electron layer*

We rescale the equations again to find the solution on electron scales, defining

$$y = \frac{\xi}{\lambda\epsilon} = \frac{x}{\delta\epsilon}. \tag{4.18}$$

The equations are

$$\Phi'' = \frac{i\epsilon y\Psi''}{1+i\alpha\epsilon y} - \frac{1}{\lambda^2\epsilon^2}\frac{1-\alpha^2}{1+Z/\tau}\left(\frac{i\epsilon y\Psi''}{1+i\alpha\epsilon y}\right)'', \tag{4.19}$$

$$\lambda^2(1+i\alpha\epsilon y)\Psi - i\lambda^2\epsilon y\Phi = \frac{1-\alpha^2}{1+\tau/Z}\left[(1+i\alpha\epsilon y)^2 + Gy^2\right]\frac{\Psi''}{1+i\alpha\epsilon y}. \tag{4.20}$$

On these scales, the shear terms are small compared with the growth terms. Dividing (4.20) by y, differentiating twice and substituting for Φ'' using (4.19), we obtain an equation for Ψ

$$\lambda^2\left[(1/y + i\alpha\epsilon)\,\Psi\right]'' + \lambda^2\epsilon^2\frac{\Psi''}{1/y+i\alpha\epsilon} = \frac{1-\alpha^2}{1+\tau/Z}\left[\left(G + \frac{\tau}{Z} + \frac{1}{y^2}(1+i\alpha\epsilon y)^2\right)\frac{\Psi''}{1/y+i\alpha\epsilon}\right]''. \tag{4.21}$$

Anticipating $\lambda \sim \epsilon$, we can now solve order by order. At lowest order, using (4.20), we have $\Psi_0'' = 0$, and so from (4.19) we also have $\Phi_0'' = 0$. To match the solution at larger scales, the lowest-order solution must be real and even, and we have

$$\Psi_0 = \Psi_{0e}, \quad \Phi_0 = \Phi_{0e}, \tag{4.22}$$

both constants. At first order, $\Psi_1'' = 0$, and we take $\Psi_1 = 0$: we can absorb any even constant piece into the zeroth-order solution, and since the solution is even and real

to lowest order overall, any term linear in y must appear at order $\lambda\epsilon$ or higher. At second order, we obtain

$$\Psi_2'' = \frac{\lambda^2(1+\tau/Z)}{1-\alpha^2}\Psi_{0e}\frac{1}{(G+\tau/Z)y^2+1}, \tag{4.23}$$

so that

$$\Psi_2 = \frac{\lambda^2\sqrt{1+\tau/Z}}{1-\alpha^2}\Psi_{0e}\int_0^y \mathrm{d}z\int_0^z \frac{\mathrm{d}u\sqrt{1+\tau/Z}}{(G+\tau/Z)u^2+1}. \tag{4.24}$$

As $y\to\infty$, we then have (in terms of ξ)

$$\Psi_e \to \Psi_{0e}\left[1+\frac{\lambda\sqrt{1+\tau/Z}}{\epsilon(1-\alpha^2)}I_G\xi - \frac{\lambda^2\sqrt{1+\tau/Z}}{1-\alpha^2}\log(\xi)\right], \tag{4.25}$$

where

$$I_G = \int_0^\infty \frac{\mathrm{d}y\sqrt{1+\tau/Z}}{(G+\tau/Z)y^2+1}. \tag{4.26}$$

If we had assumed isothermal electrons ($G=1$), $I_G=\pi/2$. The solution for Φ can be found by integrating (4.19) twice

$$\Phi = \Phi_{0e} - \frac{1}{\lambda^2\epsilon^2}\frac{1-\alpha^2}{1+Z/\tau}\left(\frac{i\epsilon y\Psi''}{1+i\alpha\epsilon y}\right) + i\epsilon\int_0^y \mathrm{d}z\int_0^z \mathrm{d}u\frac{u\Psi''}{1+i\alpha\epsilon u}. \tag{4.27}$$

The second term on the right-hand side, resulting from the small-scale asymptotic of $1-\hat{\Gamma}_0$, is dominant for $y\sim 1$, but always decays for $y\gg 1$, since Ψ'' (e.g. Ψ_2'') is strongly peaked on the electron scales. The final term on the right-hand side does produce terms in the solution for Φ that do not decay as $y\to\infty$: however, note that they are still a factor ϵ smaller than the corresponding terms in Ψ. Inserting Ψ_2'' into (4.27), the lowest-order piece is, as $y\to\infty$ and in terms of ξ,

$$\Phi_e \to \Phi_{0e} + i\epsilon\int_0^y \mathrm{d}z\int_0^z \mathrm{d}u u\Psi_2'' \to \Phi_{0e} + \frac{i\lambda(1+\tau/Z)}{1-\alpha^2}\Psi_{0e}\left[\xi\log(\xi)-\xi+\text{const.}\right] + \frac{i\lambda\Psi_{0e}}{1+Z/\tau}\frac{1}{\xi}, \tag{4.28}$$

so the non-constant piece of Φ_e is $O(\lambda)$ for $\xi\sim 1$.

Finally, if we were to solve to third order for Ψ, we could determine the odd part of the eigenmode in terms of the even one, and thus determine the small imaginary part of the solution: because this appears at third order, the linear term that appears in the asymptotic solution as $y\to\infty$ is $\sim\lambda\xi$, showing that the imaginary part of the eigenmode is a factor of around λ smaller than the real part. However, this is not necessary to obtain the growth rate.

5. Matching and dispersion relation

We can now match the ion and electron solutions. We match the constant and linear terms from $\xi\to 0$ from the ion solution (4.16 and 4.17) and $y\to\infty$ in the electron solution (4.25 and 4.28), assuming $\Delta'\delta_{in}\sim 1$. From the constant terms of Ψ, we obtain

$$\Psi_{0e} = \Psi_\infty + C_i. \tag{5.1}$$

As we found above, at lowest order the leading non-constant terms of Φ_e are $O(\lambda)$, and so to lowest order, the linear term in (4.17) must be zero

$$\frac{1}{2}\alpha\Delta'\delta_{in}\Psi_\infty - \frac{1}{\alpha}C_i\left[1 - \frac{1-\alpha^2}{1+Z/\tau}\right] = 0, \tag{5.2}$$

whence

$$C_i = \frac{\frac{1}{2}\alpha^2\Delta'\delta_{in}\Psi_\infty(1+Z/\tau)}{Z/\tau+\alpha^2}. \tag{5.3}$$

The $O(\lambda)$ terms of Φ_e in (4.28) can in principle be matched with the next-order solution to Φ_i (which we have not calculated), providing a small correction to our results, but we do not attempt this here. Finally, matching the linear terms for Ψ_i as $\xi \to 0$ (4.16) and Ψ_e as $y \to \infty$ (4.25)

$$\frac{1}{2}\Delta'\delta_{in}\Psi_\infty - C_i = \frac{\lambda\sqrt{1+\tau/Z}}{\epsilon(1-\alpha^2)}I_G\Psi_{0e}. \tag{5.4}$$

Inserting (5.1) and (5.3), we obtain the dispersion relation

$$\lambda = \frac{\frac{1}{2}\Delta'\delta_{in}\epsilon(1-\alpha^2)^2 Z/\tau}{Z/\tau+\alpha^2+\frac{1}{2}\alpha^2\Delta'\delta_{in}(1+Z/\tau)}\frac{1}{I_G\sqrt{1+\tau/Z}}. \tag{5.5}$$

5.1. *Growth rate*

Using the definitions of λ (4.7) and δ (4.1), the growth rate is

$$\frac{\gamma a}{v_{Ay}} = \frac{k\Delta'\delta_{in}^2\epsilon(1-\alpha^2)^2}{2I_G\sqrt{1+\tau/Z}(1+\alpha^2\tau/Z+\frac{1}{2}\alpha^2\Delta'\delta_{in}(1+\tau/Z))}. \tag{5.6}$$

Inserting δ_{in} (4.15), we find that

$$\frac{\gamma a}{v_{Ay}} \sim \begin{cases} k\Delta'\rho_s \mathrm{d}_e \dfrac{(1-\alpha^2)\sqrt{1+\tau/Z)}}{2I_G(1+\alpha^2\tau/Z)}, & \Delta'\delta_{in} \ll 1 \\ k\mathrm{d}_e\dfrac{(1-\alpha^2)^{3/2}}{\alpha^2 I_G(1+\tau/Z)}, & \Delta'\delta_{in} \gg 1. \end{cases} \tag{5.7}$$

The growth rate for $\Delta'\delta_{in} \ll 1$ has the same scaling with d_e and ρ_s as the no-flow scaling (1.1), but for $\Delta'\delta_{in} \gg 1$, we have obtained the surprising result that the growth rate is independent of ρ_s: in the no-flow case, we had $\gamma_0 \propto \rho_s^{2/3}\mathrm{d}_e^{1/3}$. Note that the growth rate for $\Delta'\delta_{in} \gg 1$ does not match smoothly onto the no-flow scaling (1.1): this is because the expansion in the ion region is invalidated for $\alpha \ll \lambda$ (see § 5.2 below).

The transition between these scalings occurs where they match. Inserting $\Delta' a \propto 1/(ka)^n$ (see § 1.1), the transition occurs roughly at

$$k_{tr}a \sim (\rho_s/a)^{1/n}\frac{\alpha^{2/n}}{(1-\alpha^2)^{1/2n}}\left(\frac{(1+\tau/Z)^{3/2}}{1+\alpha^2\tau/Z}\right)^{1/n}, \tag{5.8}$$

for which the growth rate is of order

$$\frac{\gamma_{tr}a}{v_{Ay}} \sim \frac{\rho_s^{1/n}d_e}{a^{1+1/n}}\frac{(1-\alpha^2)^{3/2-1/2n}}{\alpha^{2-2/n}}\frac{(1+\tau/Z)^{3/2n-1}}{(1+\alpha^2\tau/Z)^{1/n}}. \tag{5.9}$$

For $n=2$, the growth rate increases with k for $\Delta'\delta_{in}\gg 1$ and decreases with k for $\Delta'\delta_{in}\ll 1$, so that γ_{tr} is also the maximum growth rate, occuring uniquely at k_{tr}. For the $n=1$ case, γ is independent of k for $\Delta'\delta_{in}\ll 1$, and equal to γ_{tr} for all $k>k_{tr}$.

This differs in several ways from the growth rate for $\alpha=0$ (1.1). First, the growth rate scales strongly with $1-\alpha^2$: as $\alpha\to 1$, the growth rate vanishes, as is the case for the resistive MHD tearing mode with shear (Hofman 1975; Chen & Morrison 1989; Boldyrev & Loureiro 2018; Shi *et al*. 2021*a*), where $\gamma_{MHD}\propto(1-\alpha^2)^{1/2}$: thus the growth rate of the tearing mode is more strongly suppressed in a collisionless plasma than in resistive MHD.[2] Second, the growth rate depends differently on τ. For $\tau\ll 1$, the growth rate becomes independent of τ, similarly to the tearing mode without flow shear. In contrast, for $\tau\gg 1$, the maximum growth rate is proportional to $\tau^{(1/2n)-1}$; the opposite dependency to the case without flow shear, for which $\gamma_{0tr}\propto\tau^{1/2}$ for $\tau\gg 1$. Finally, in general the growth rate also depends differently on the scales ρ_s and d_e than in the no-flow case: without shear flow, $\gamma_{0tr}\propto \mathrm{d}_e^{1/3+2/3n}\rho_s^{2/3+1/3n}$, but with shear flow, $\gamma_{tr}\propto \mathrm{d}_e\rho_s^{1/n}$. For $n=1$, these scalings coincide, but for $n=2$, $\gamma_{tr}/\gamma_{0tr}\propto\epsilon^{1/3}$, where $\epsilon=\mathrm{d}_e/\rho_s\ll 1$.

5.2. *Validity and the small shear flow limit*

For the expansion in the ion region to be valid, we must have $\lambda\ll\alpha$. For $\Delta'\delta_{in}\ll 1$, this is easily satisfied, and indeed, the growth rate in this case smoothly joins onto the no-flow growth rate (1.1) as $\alpha\to 0$. For $\Delta'\delta_{in}\gg 1$, the inequality is

$$\frac{\epsilon(1-\alpha^2)^2}{\alpha^2(1+\tau/Z)^{3/2}}\ll\alpha, \tag{5.10}$$

or α above a critical α_c defined by

$$\frac{\alpha_c}{(1-\alpha_c^2)^{2/3}}=\epsilon^{1/3}(1+\tau/Z)^{-1/2}. \tag{5.11}$$

For $\epsilon\ll 1$, $\alpha_c\sim\epsilon^{1/3}$. Taking $\beta_e\approx 0.1$ in the low-β solar wind and corona, $\epsilon\approx 0.1$ and $\alpha_c\approx 0.5$. Thus, even a modest shear flow (far enough from $\alpha=1$ that $1-\alpha^2$ is not small) can affect the growth rate scalings with d_e and ρ_s for $\Delta'\delta_{in}\gg 1$. This is because the growth rate of the mode is slow compared with the shearing rate on the ion scales.

6. Numerical tests

We use an eigenvalue code to solve (2.13–2.14) assuming cold ions and isothermal electrons (and thus we do not need to solve (2.15)): these assumptions (while unjustified physically for the case of the solar wind) make the equations much simpler to solve numerically. We use the profile (Loureiro *et al*. 2005)

$$f(x/a)=-2\tanh(x/a)\mathrm{sech}^2(x/a). \tag{6.1}$$

For $ka\ll 1$, $\Delta' a\sim 15/(ka)^2$; i.e. $n=2$. For this profile, the maximum growth rate is attained uniquely at the transitional wavenumber, rather than for all $k>k_{tr}$ as would be the case for the more usual $f(x/a)=\tanh(x/a)$ profile, for which $n=1$.

[2]For $\alpha^2>1$, we would have instead the Kelvin–Helmholtz instability: since $a\gg\rho_i$ this is essentially the same as the MHD case (Miura & Pritchett 1982).

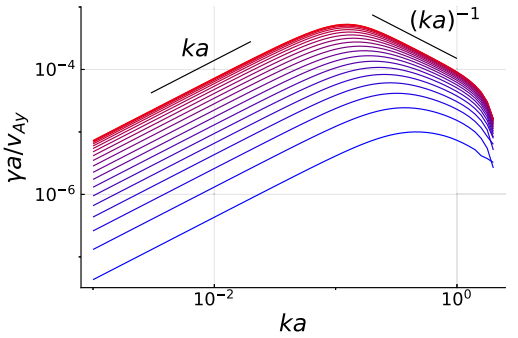

FIGURE 1. Growth rate as a function of ka for $\alpha = 0, 0.05, \ldots, 0.95$, red to blue lines. We set $\rho = 0.01a$ and $\mathrm{d}_e = 0.001a$.

Growth rates as a function of k for different α are shown in figure 1, showing the expected scalings with k for both small and large k (large and small Δ'). Because the transition moves to larger k with increasing shear flow, the interval in k over which the small-Δ' scalings are relevant gets narrower as α increases towards 1.

We plot growth rates at fixed k as a function of $1-\alpha^2$ in figure 2. For both small and large Δ' (top left and right panels, respectively), the scalings agree with (5.7). In the top right panel, we have also marked on the x-axis the position at which $\alpha = \epsilon^{1/3}$: for smaller α (larger $1-\alpha^2$), we do not expect our scaling to apply – and indeed, the behaviour changes at around this point. The maximum/transitional growth rate (5.9) and corresponding transitional wavenumber (5.8) are shown in the bottom panels, and also agree quite well with the predicted scalings, shown as black lines.

We also check the dependence of the growth rate on both ρ_s and d_e. As a reminder, for $\alpha = 0$ the dependencies are given by (1.1) with $\tau = 0$: our code reproduces these scalings (not shown). In figure 3 we plot the scalings for $\alpha = 0.9$. For large Δ', the growth rate depends linearly on d_e, and does not depend on ρ_s: both as predicted (5.7), and very different to the $\alpha = 0$ case. For small Δ', at a wavenumber of $ka = 1.12$, the growth rate depends on the product $\mathrm{d}_e\rho_s$, as in the no-flow case, also in agreement with our predictions.

We can also check the behaviour of the width of the perturbed current profile: this corresponds to the scale at which the electron terms become important, $x \sim \delta\epsilon$. We have checked that this agrees with the scalings found numerically for the growth rate.

7. Conclusions

We have studied the collisionless tearing mode in the presence of significant shear flows, as parametrised by $\alpha = \delta u/\delta b$, where δu and δb are the amplitudes of the background velocity and magnetic field fluctuations, pointing in the y (or L) direction and varying in the x (or N) direction across the current sheet. We find that the growth rates depend strongly on α, with a maximum growth rate given by (5.9),

$$\frac{\gamma_{tr} a}{v_{Ay}} \sim \frac{\rho_s^{1/n}\mathrm{d}_e}{a^{1+1/n}} \frac{(1-\alpha^2)^{3/2-1/2n}}{\alpha^{2-2/n}} \frac{(1+\tau/Z)^{3/2n-1}}{(1+\alpha^2\tau/Z)^{1/n}}, \tag{7.1}$$

where $n = 1$ (e.g. for a Harris-type profile) or $n = 2$ (e.g. for a sinusoidal type profile). As $\alpha \to 1$ (an exactly Alfvénic flow), $\gamma \to 0$. Moreover, for large ion-to-electron

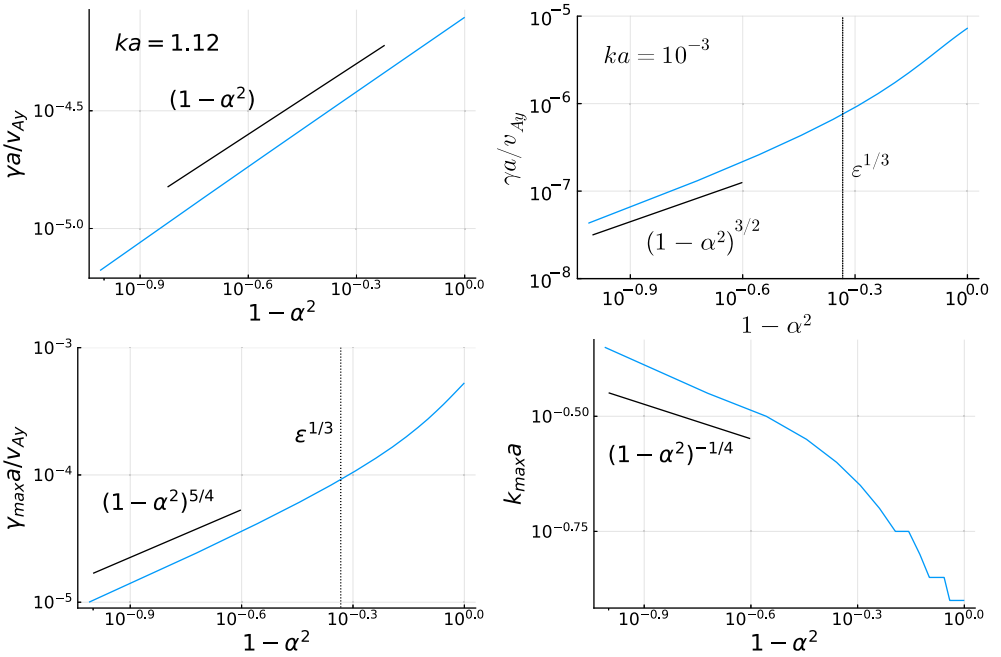

FIGURE 2. Top left: γ for $ka = 1.12$, at which wavenumber $\Delta'\delta_{in} \ll 1$. Top right: γ for $ka = 10^{-3}$ ($\Delta'\delta_{in} \gg 1$). Bottom left: maximum growth rate γ_{max}. Bottom right: the wavenumber k_{tr} at which γ_{max} is attained. The vertical dashed lines on the top right and bottom left panels mark $\alpha = \epsilon^{1/3}$.

temperature ratios, $\tau = T_{0i}/T_{0e}$, the growth rate decreases with τ, $\gamma_{tr} \propto \tau^{1/2n-1}$. With $n = 1$ for simplicity, relative to the maximum tearing mode growth rate with $\alpha = 0$, γ_{0tr} (see (1.2)), we have

$$\frac{\gamma_{tr}}{\gamma_{0tr}} = \frac{1-\alpha^2}{1+\alpha^2\tau/Z}. \tag{7.2}$$

As described in the introduction, a remarkable absence of reconnection was reported in the near-Sun solar wind observed during PSP's first perihelion (Phan *et al*. 2020). This has been confirmed in a comprehensive recent study of the PSP data by Eriksson *et al*. (2024), who found that reconnection was extremely rare more specifically in faster, high-ion-temperature solar wind emerging from coronal holes: this is also the wind that is typically highly Alfvénic (D'Amicis & Bruno 2015; D'Amicis *et al*. 2021), with highly correlated velocity and magnetic field fluctuations, $\delta u \sim \pm\delta b$ or $1-\alpha^2 \ll 1$ (Ervin *et al*. 2024). Typically, this wind also has large $\tau = T_{0i}/T_{0e}$ (Shi *et al*. 2023), probably due to higher ion heating in imbalanced turbulence due to the recently discovered helicity barrier (Meyrand *et al*. 2021; Squire *et al*. 2022). Similar clustering was observed at larger heliocentric distances by Fargette *et al*. (2023), possibly with the same underlying cause.

We have shown that both these parameters typical of the Alfvénic wind, $1-\alpha^2 \ll 1$ and $\tau \gtrsim 1$, suppress the tearing mode growth rate, and thus increase the reconnection onset time, comparable to γ^{-1}. We can roughly estimate a typical reconnection time from our expression for the growth rate: taking $n = 1$ and typical values for the PSP Alfvénic wind, $\alpha \approx 0.9$ and $\tau \approx 2$ (Chen *et al*. 2020;

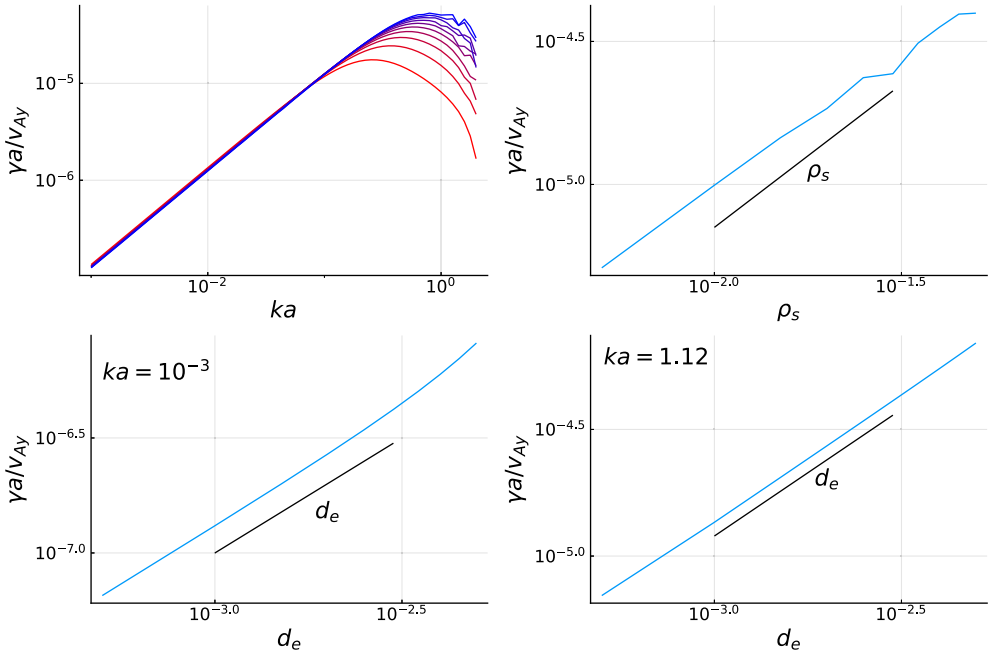

FIGURE 3. In all panels $\alpha = 0.9$. Top left: growth rate vs k, different lines correspond to different ρ_s. For large $\Delta'\delta_{in}$ (smaller wavenumbers), the growth rate is independent of ρ_s. Top right: growth rate as a function of ρ_s for $ka = 1.12$, i.e. for $\Delta'\delta_{in} \ll 1$. Bottom left: growth rate as a function of d_e for $ka = 10^{-3}$, i.e. $\Delta'\delta_{in} \gg 1$. Bottom right: growth rate as a function of d_e for $ka = 1.12$.

Shi *et al*. 2021*b*, 2023; Ervin *et al*. 2024), we find $\gamma_{tr}/\gamma_{0tr} \approx 0.07$. On the other hand, the eddy turnover time $\tau_{nl} \sim \lambda/\delta u(1-\alpha^2)$ in imbalanced turbulence is increased by the same factor $(1-\alpha^2)^{-1}$ (Schekochihin 2022), so if all the current sheets are produced by turbulence, the product $\gamma_{tr}\tau_{nl}$ is left relatively unchanged. If the development of current sheets is controlled by the eddy turnover time, then the overall prevalence of reconnection would not be suppressed by this mechanism. However, it is far from clear that this is the only time scale available. For example, sharp switchback boundaries may evolve instead due to the large-scale inhomogeneity in the system, on the solar wind expansion time of order $\tau_{exp} \sim R/U_{sw}$, where R is the radial distance from the Sun and U_{sw} is the solar wind velocity (Mallet *et al*. 2021).

Our work could be extended in several important ways to better describe the solar wind current sheets. First, KREHM cannot handle large equilibrium flows, and we are therefore limited to guide-field reconnection. Second, we have not allowed an equilibrium parallel flow shear, which is also often observed in the solar wind (Eriksson *et al*. 2024). Third, KREHM is formally limited to small β. This is perhaps reasonable for the solar wind close to the Sun, but further out in the heliosphere β is typically of order unity. Finally, we have also not allowed an equilibrium density gradient (again, often observed in the data), which can suppress reconnection (Swisdak *et al*. 2003) and also requires a more careful treatment of the matching between the ion and outer layers (Connor *et al*. 2019). Nevertheless, our theory may help to explain the patchy suppression of reconnection in the PSP data, but further work is needed to generalise the equilibrium and to elucidate the formation time scale of the observed sheet-like structures.

Acknowledgements

The authors would like to thank the anonymous reviewers for helpful comments that significantly improved the paper. A.M., S.E. and M.S. were supported by NASA grant 80NSSC20K1284. J.J. was funded by the U.S. Department of Energy under Contract No. DE-AC 02–09CH1146 via an LDRD grant.

Editor Nuno Loureiro thanks the referees for their advice in evaluating this article.

Declaration of interests

The authors report no conflict of interest.

REFERENCES

BIRN, J. et al. 2001 Geospace environmental modeling (gem) magnetic reconnection challenge. *J. Geophys. Res.: Space Phys.* **106** (A3), 3715–3719.

BOLDYREV, S. & LOUREIRO, N.F. 2018 Calculations in the theory of tearing instability. *J. Phys.: Conf. Ser.* **1100** (1), 012003.

CASSAK, P.A. 2011 Theory and simulations of the scaling of magnetic reconnection with symmetric shear flow. *Phys. Plasmas* **18** (7), 072106.

CHAPMAN, SYDNEY & KENDALL, P.C. 1963 Liquid instability and energy transformation near a magnetic neutral line: a soluble non-linear hydromagnetic problem. *Proc. R. Soc. Lond. (A) Math. Phys. Sci.*, **271** (1347), 435–448.

CHEN, C.H.K. et al. 2020 The evolution and role of solar wind turbulence in the inner heliosphere. *Astrophys. J.* **246** (2), 53.

CHEN, X.L. & MORRISON, P.J. 1989 Resistive tearing instability with equilibrium shear flow. *Phys. Fluids B* **2** (3), 495–507.

COMISSO, L., HUANG, Y.-M., LINGAM, M., HIRVIJOKI, E. & BHATTACHARJEE, A. 2018 Magnetohydrodynamic turbulence in the plasmoid-mediated regime. *Astrophys. J.* **854** (2), 103.

CONNOR, J.W., HAM, C.J., HASTIE, R.J. & ZOCCO, A. 2019 Ion landau damping and drift tearing modes. *J. Plasma Phys.* **85** (2), 905850204.

D'AMICIS, R., ALIELDEN, K., PERRONE, D., BRUNO, R., TELLONI, D., RAINES, J.M., LEPRI, S.T. & ZHAO, L. 2021 Solar wind Alfvénicity during solar cycle 23 and 24-perspective for future observations with parker solar probe and solar orbiter. *Astron. Astrophys.* **654**, A111.

D'AMICIS, R. & BRUNO, R. 2015 On the origin of highly Alfvénic slow solar wind. *Astrophys. J.* **805** (1), 84.

ERIKSSON, S., SWISDAK, M., MALLET, A., KRUPAROVA, O., LIVI, R., ROMEO, O., BALE, S.D., KASPER, J.C., LARSON, D.E. & PULUPA, M. 2024 Parker solar probe observations of magnetic reconnection exhausts in quiescent plasmas near the sun. *Astrophys. J.* **965** (1), 76.

ERIKSSON, S., SWISDAK, M., WEYGAND, J.M., MALLET, A., NEWMAN, D.L., LAPENTA, G., WILSON III, L.B., TURNER, D.L. & LARSEN, B. 2022 Characteristics of multi-scale current sheets in the solar wind at 1 au associated with magnetic reconnection and the case for a heliospheric current sheet avalanche. *Astrophys. J.* **933** (2), 181.

ERVIN, T., BALE, S.D., BADMAN, S.T., RIVERA, Y.J., ROMEO, O., HUANG, J., RILEY, P., BOWEN, T.A., LEPRI, S.T. & DEWEY, R.M. 2024 Compositional metrics of fast and slow Alfvénic solar wind emerging from coronal holes and their boundaries. *Astrophys. J.* **969** (2), 83.

FARGETTE, N. et al. 2023 Clustering of magnetic reconnection exhausts in the solar wind: an automated detection study. *Astron. Astrophys.* **674**, A98.

HARRIS, E.G. 1962 On a plasma sheath separating regions of oppositely directed magnetic field. *Nuovo Cimento* **23** (1), 115–121.

HOFMAN, I. 1975 Resistive tearing modes in a sheet pinch with shear flow. *Plasma Phys.* **17** (2), 143–157.

JI, H. et al. 2023 Laboratory study of collisionless magnetic reconnection. *Space Sci. Rev.* **219** (8), 76.

KADOMTSEV, B.B. 1975 Disruptive instability in tokamaks. *Sov. Tech. Phys. Lett.* **1** (5), 389–391.

LOTEKAR, A.B., VASKO, I.Y., PHAN, T., BALE, S.D., BOWEN, T.A., HALEKAS, J., ARTEMYEV, A.V., KHOTYAINTSEV, YU V. & MOZER, F.S. 2022 Kinetic-scale current sheets in near-sun solar wind: properties, scale-dependent features and reconnection onset. *Astrophys. J.* **929** (1), 58.

LOUREIRO, N.F. & BOLDYREV, S. 2017*a* Role of magnetic reconnection in MHD turbulence. *Phys. Rev. Lett.* **118** (24), 245101.

LOUREIRO, N.F. & BOLDYREV, S. 2017*b* Collisionless reconnection in magnetohydrodynamic and kinetic turbulence. *Astrophys. J.* **850** (2), 182.

LOUREIRO, N.F., COWLEY, S.C., DORLAND, W.D., HAINES, M.G. & SCHEKOCHIHIN, A.A. 2005 X-point collapse and saturation in the nonlinear tearing mode reconnection. *Phys. Rev. Lett.* **95** (23), 235003.

MALLET, A., SCHEKOCHIHIN, A.A. & CHANDRAN, B.D.G. 2017*b* Disruption of Alfvénic turbulence by magnetic reconnection in a collisionless plasma. *J. Plasma Phys.* **83** (6), 905830609.

MALLET, A., SCHEKOCHIHIN, A.A. & CHANDRAN, B.D.G. 2017*a* Disruption of sheet-like structures in Alfvénic turbulence by magnetic reconnection. *Mon. Not. R. Astron. Soc.* **468** (4), 4862–4871.

MALLET, A., SQUIRE, J., CHANDRAN, B.D.G., BOWEN, T. & BALE, S.D. 2021 Evolution of large-amplitude Alfvén waves and generation of switchbacks in the expanding solar wind. *Astrophys. J.* **918** (2), 62.

MEYRAND, R., SQUIRE, J., SCHEKOCHIHIN, A.A. & DORLAND, W. 2021 On the violation of the zeroth law of turbulence in space plasmas. *J. Plasma Phys.* **87** (3), 535870301.

MIURA, AKIRA & PRITCHETT, P.L. 1982 Nonlocal stability analysis of the MHD Kelvin-Helmholtz instability in a compressible plasma. *J. Geophys. Res.: Space Phys.* **87** (A9), 7431–7444.

PASCHMANN, G., ØIEROSET, M. & PHAN, T. 2013 In-situ observations of reconnection in space. *Space Sci. Rev.* **178** (2-4), 385–417.

PEGORARO, F. & SCHEP, T.J. 1986 Theory of resistive modes in the ballooning representation. *Plasma Phys. Control. Fusion* **28** (4), 647–667.

PHAN, T.D. 2020 Parker solar probe in situ observations of magnetic reconnection exhausts during encounter 1. *Astrophys. J. Suppl.* **246** (2), 34.

PUCCI, F. & VELLI, M. 2014 Reconnection of quasi-singular current sheets: the "Ideal" tearing mode. *Astrophys. J. Lett.* **780** (2), L19.

SCHEKOCHIHIN, A.A. 2022 MHD turbulence: a biased review. *J. Plasma Phys.* **88** (5), 155880501.

SHAY, M.A., DRAKE, J.F., ROGERS, B.N. & DENTON, R.E. 2001 Alfvénic collisionless magnetic reconnection and the hall term. *J. Geophys. Res.: Space Phys.* **106** (A3), 3759–3772.

SHI, C., ARTEMYEV, A., VELLI, M. & TENERANI, A. 2021*a* Stability of the magnetotail current sheet with normal magnetic field and field-aligned plasma flows. *J. Geophys. Res.: Space Phys.* **126** (11), e2021JA029711.

SHI, CHEN et al. 2023 Proton and electron temperatures in the solar wind and their correlations with the solar wind speed. *Astrophys. J.* **944** (1), 82.

SHI, CHEN et al. 2021*b* Alfvénic versus non-Alfvénic turbulence in the inner heliosphere as observed by Parker Solar Probe. *Astron. Astrophys.* **650**, A21.

SQUIRE, J., MEYRAND, R., KUNZ, M.W., ARZAMASSKIY, L., SCHEKOCHIHIN, A.A. & QUATAERT, E. 2022 High-frequency heating of the solar wind triggered by low-frequency turbulence. *Nat. Astron.* **6** (6), 715–723.

SWISDAK, M., ROGERS, B.N., DRAKE, J.F. & SHAY, M.A. 2003 Diamagnetic suppression of component magnetic reconnection at the magnetopause. *J. Geophys. Res.: Space Phys.* **108** (A5), 1218.

TOLMAN, E.A., LOUREIRO, N.F. & UZDENSKY, D.A. 2018 Development of tearing instability in a current sheet forming by sheared incompressible flow. *J. Plasma Phys.* **84** (1), 905840115.

UZDENSKY, D.A. & LOUREIRO, N.F. 2016 Magnetic reconnection onset via disruption of a forming current sheet by the tearing instability. *Phys. Rev. Lett.* **116** (10), 105003.

VASKO, I.Y., ALIMOV, K., PHAN, T., BALE, S.D., MOZER, F.S. & ARTEMYEV, A.V. 2022 Kinetic-scale current sheets in the solar wind at 1 au: scale-dependent properties and critical current density. *Astrophys. J. Lett.* **926** (2), L19.

YAN, XIAOLI et al. 2022 Fast plasmoid-mediated reconnection in a solar flare. *Nat. Commun.* **13** (1), 640.

ZANINI, M. et al. 2020 ECCD-induced sawtooth crashes at W7-X. *Nucl. Fusion* **60** (10), 106021.

ZOCCO, A. & SCHEKOCHIHIN, A.A. 2011 Reduced fluid-kinetic equations for low-frequency dynamics, magnetic reconnection, and electron heating in low-beta plasmas. *Phys. Plasmas* **18** (10), 102309.